Bioactive Materials 40 (2024) 34–46

Contents lists available at ScienceDirect

Bioactive Materials

journal homepage: www.keaipublishing.com/en/journals/bioactive-materials

Biodegradable high-nitrogen iron alloy anastomotic staples: *In vitro* and *in vivo* studies

Sihan Lu [b,1], Peng Wang [c,1], Qingchuan Wang [a,**], Peng Deng [d], Yonghui Yuan [e], Xiaoqing Fu [a], Yinghui Yang [f], Lili Tan [a], Ke Yang [a,***], Xun Qi [g,*]

[a] *Institute of Metal Research, Chinese Academy of Sciences, Shenyang, 110016, China*
[b] *School of Intelligent Medicine, China Medical University, Shenyang, 110122, China*
[c] *Department of Interventional Therapy, The First Hospital of China Medical University, Shenyang, 110001, China*
[d] *Department of Surgical Oncology and General Surgery, The First Hospital of China Medical University, Shenyang, 110001, China*
[e] *Cancer Hospital of China Medical University, Liaoning Cancer Hospital & Institute, Clinical Research Center for Malignant Tumor of Liaoning Province, Shenyang, 110801, China*
[f] *Silvan Medical Device Co., Ltd., Suzhou, 215004, China*
[g] *Key Laboratory of Diagnostic Imaging and Interventional Radiology of Liaoning Province, Department of Radiology, The First Hospital of China Medical University, Shenyang, 110001, China*

ARTICLE INFO

Keywords:
High-nitrogen
Iron alloy
Surgical staples
Mechanical property
Degradation

ABSTRACT

For gastrointestinal anastomosis, metallic biodegradable staples have a broad application potential. However, both magnesium and zinc alloys have relatively low strength to withstand the repeated peristalsis of the gastrointestinal tract. In this study, we developed a novel kind of biodegradable high-nitrogen iron (HN–Fe) alloy wires (0.23 mm), which were fabricated into the staples. The tensile results showed that the ultimate tensile strength and elongation of HN–Fe wires were 1023.2 MPa and 51.0 %, respectively, which was much higher than those of other biodegradable wires. The degradation rate *in vitro* of HN–Fe wires was slightly higher than that of pure Fe wires. After 28 days of immersion, the tensile strength of HN–Fe wires remained not less than 240 MPa, meeting the clinical requirements. Furthermore, sixteen rabbits were enrolled to conduct a comparison experiment using HN–Fe and clinical Ti staples for gastroanastomosis. After 6 months of implantation, a homogeneous degradation product layer on HN–Fe staples was observed and no fracture occurred. The degradation rate of HN–Fe staples *in vivo* was significantly higher than that *in vitro*, and they were expected to be completely degraded in 2 years. Meanwhile, both benign cutting and closure performance of HN–Fe staples ensured that all the animals did not experience hemorrhage and anastomotic fistula during the observation. The anastomosis site healed without histopathological change, inflammatory reaction and abnormal blood routine and biochemistry, demonstrating good biocompatibility of HN–Fe staples. Thereby, the favorable performance makes the HN–Fe staples developed in this work a promising candidate for gastrointestinal anastomosis.

1. Introduction

Globally, the incidence of gastrointestinal cancers accounts for over 25 % of all cancer cases and contributes to approximately 33 % of cancer-related deaths [1]. At present, surgical resection is the main means of curative treatment for gastrointestinal tumors. Gastrointestinal anastomosis is crucial and commonly associated with a higher reoperation rate and an increased risk of postoperative morbidity and mortality [2]. Since the 1980s, an increasing number of staplers have been used in gastrointestinal surgery to reduce postoperative complications [3]. The stapler replaces the complex operation of manual suturing, reducing the time for surgery and gastrointestinal exposure, and

Peer review under responsibility of KeAi Communications Co., Ltd.
* Corresponding author. Nanjing North Street, Heping District, Shenyang, Liaoning, 110001, China.
** Corresponding author. Wenhua Road, Shenyang, Liaoning, 110016, China.
*** Corresponding author.
E-mail addresses: qcwang11s@imr.ac.cn (Q. Wang), kyang@imr.ac.cn (K. Yang), qixun716@hotmail.com (X. Qi).
[1] Sihan Lu and Peng Wang have contributed equally to the work.

https://doi.org/10.1016/j.bioactmat.2024.06.005
Received 30 December 2023; Received in revised form 26 April 2024; Accepted 1 June 2024

resulting in a shorter recovery time for the gastrointestinal system after surgery [4]. According to the standard of YY 0876–2013, the tensile strength of the material to be made into anastomosis staples should not be less than 240 MPa. As representatives of non-absorbable mechanical anastomosis materials, titanium (Ti) and its alloys have been widely used in gastrointestinal staples due to their superior mechanical properties [5]. However, the bioinert Ti can cause local tissue inflammation and affect the medical image observation, and due to gastrointestinal peristalsis, Ti-staples may cause damage to surrounding tissues and lead to other complications [6].

In the field of medical implants, biodegradable materials have garnered significant attention in recent years. Biodegradable surgical sutures, which were made by polydioxanone, polylactic, and polyglycolic acid, have been applied in clinical practice and effectively reduce the side effects caused by permanent materials [7–9]. However, the mechanical properties of these polymers are too low to provide adequate mechanical support. In contrast, the most obvious advantage of metallic materials is their superior mechanical properties. Based on these, increasing efforts were paid to develop new biodegradable metal gastrointestinal staples.

Currently, biodegradable metals mainly include magnesium (Mg), zinc (Zn), iron (Fe) and their alloys. Considerable attention has been dedicated to the assessment of their mechanical, degradation, and biological performance [10,11]. Different types of biodegradable alloys have their own characteristics [12]: (1) Mg alloys have the advantages of good biocompatibility and magnetic resonance imaging (MRI) compatibility, but it undergoes hydrogen evolution degradation with an extremely fast degradation rate and poor mechanical properties; (2) Fe alloys have good processability, the highest mechanical strength and acceptable biocompatibility, but its degradation rate is slow; (3) The degradation rate of Zn alloys is between that of Mg alloys and Fe alloys, but the mechanical properties are insufficient. Numerous efforts have been devoted to evaluating biological effects of Mg alloy and Zn alloy gastrointestinal staples. Guo et al. [13] fabricated Zn–Li–Mn alloy staples, which were used for gastrointestinal anastomosis in pig models, and were expected to be completely degraded in about 1 year. The gastrointestinal tissue was healed after 12 weeks, and Zn–Li–Mn alloy staples demonstrated good biocompatibility. Moreover, the challenges pertaining to the aging and creep of Zn alloys at ambient temperature remain unresolved impediments for their practical utilization [6]. Wu et al. developed biodegradable high purity Mg staples for gastric anastomosis, and the *in vivo* experiment indicated good biocompatibility of the Mg staples [14]. Notably, the Mg alloy staple degrades rapidly and is expected to degrade completely in 3 months, and further exploration for the appropriate degradation period of the implant that matches the tissue healing and mechanical properties is still needed [6,15].

Compared to Mg alloys and Zn alloys, Fe alloys have higher strength and plasticity, with particularly significant advantages in mechanical properties, and can withstand the repeated peristalsis of the gastrointestinal tract [16]. In addition, in contrast to the body fluid and blood environment, the corrosion of gastric and intestinal fluids significantly enhances the deterioration of metallic materials [17]. Exposure of Fe alloys with slower degradation rates to the gastrointestinal tract will also leave sufficient time for the healing of the anastomotic site. Studies on biodegradable Fe alloys were mainly focused on the cardiovascular application, without report on anastomotic staples.

Their pioneering study not only affirms the biological functions and biosafety of biodegradable Fe alloys, but also points out the issues that need to be addressed in current Fe alloy materials. Peuster et al. successfully implanted a pure Fe stent into the descending aorta of New Zealand white rabbits, revealing the absence of any vascular blockage attributed to inflammation, neointimal hyperplasia, or thrombosis, which provide compelling evidence for the favorable biosafety and biocompatibility of the biodegradable iron stent, but with the problem of slow degradation [18]. Subsequently, a range of non-ferromagnetic FeMn alloys, such as FeMnC [19], FeMnSi [20], FeMnPd [21] and FeMnAg [22], were developed with excellent comprehensive performance. The mechanical properties of these alloys were further improved, and the degradation rate was also slightly increased through large deformation or second phase precipitation, but often leading to the aggravation of local corrosion. Moreover, Zheng et al. developed the biodegradable nitrided Fe stent, which has been applied in clinical practice. Previous research results have shown that the stent has a fast degradation rate by precipitating nitrides, but the nitride Fe easily lead to severe localized corrosion, as well as poor MRI compatibility of its ferromagnetism due to the low nitrogen (N) content (0.08 wt%) [23,24]. Certainly, the appeal research finding provided foundations and directions for the medical application of biodegradable Fe alloys.

A series of high-N Fe alloys with a maximum N content of 0.6 wt% have been firstly developed in our previous studies by increasing the manganese (Mn) content and high-pressure smelting. This novel high-N Fe alloy obtained a non-ferromagnetic austenitic structure and an N content exceeding the solubility limitation at atmospheric pressure smelting [25]. The advantages of high-N alloying were found that the degradation rate and local corrosion resistance of Fe alloys were surprisingly increased simultaneously. Besides, the application of high-N Fe alloys with superior mechanical properties can further reduce the size of the implant to shorten the degradation period, and more importantly, also reduce the irritation to the healing site and accelerate the tissue repair [26,27].

Accordingly, based on the above promising study results, we have innovatively developed a biodegradable high-N Fe-based alloy wire with favorable mechanical strength and ductility, which meet the preparation requirements of anastomosis staples. The mechanical properties and their attenuation with time, *in vitro* and *in vivo* degradation behaviors, biocompatibility and biological functions of high-N Fe-based alloy were investigated to explore their feasibility as biodegradable staples in gastrointestinal anastomosis (Scheme 1).

2. Materials and methods

2.1. Materials and preparation

The novel biodegradable high-N Fe-based alloy, referred to as HN–Fe, was prepared under a high-pressure N_2 atmosphere of 1.5 MPa. Then, the alloy bars with diameter of 8 mm were obtained by forging at 1473 K with holding time of 2 h and hot rolling at 1423 K with holding time of 1.5 h. Finally, the HN–Fe wires with diameter of 0.23 mm were produced by multi-passes hot and cold drawings combined with annealing treatment. Inductively coupled plasma-optical emission spectrometer (ICP-OES, iCAP6300), carbon-sulfur analyzer (CS600) and oxygen-nitrogen-hydrogen analyzer (ONH836) were used to determine the alloy compositions. Commercial pure Fe wire with a purity of 99.95 % and a diameter of 0.20 mm was chosen as the control, referred to as Fe wire. The chemical composition was shown in Table 1.

All wires were ultrasonically cleaned in the acid wash solution (HCl 500 mL, methenamine 20 g, and H_2O 500 mL) to remove the oxide layer on the surfaces before the tests, since HN–Fe and Fe wires were easily oxidized in air. Subsequently, electrolytic polishing was performed in an electrolyte of 10 % perchloric acid and 90 % alcohol at 253 K and 39 V to make the surface smooth.

The anastomotic staples were made using HN–Fe wires by polishing, cutting and bending, which were further sterilized by ethylene oxide and sealed in vacuum for gastrointestinal anastomosis experiments in animals. The pure Ti anastomotic staples commonly used in clinic were used as the control.

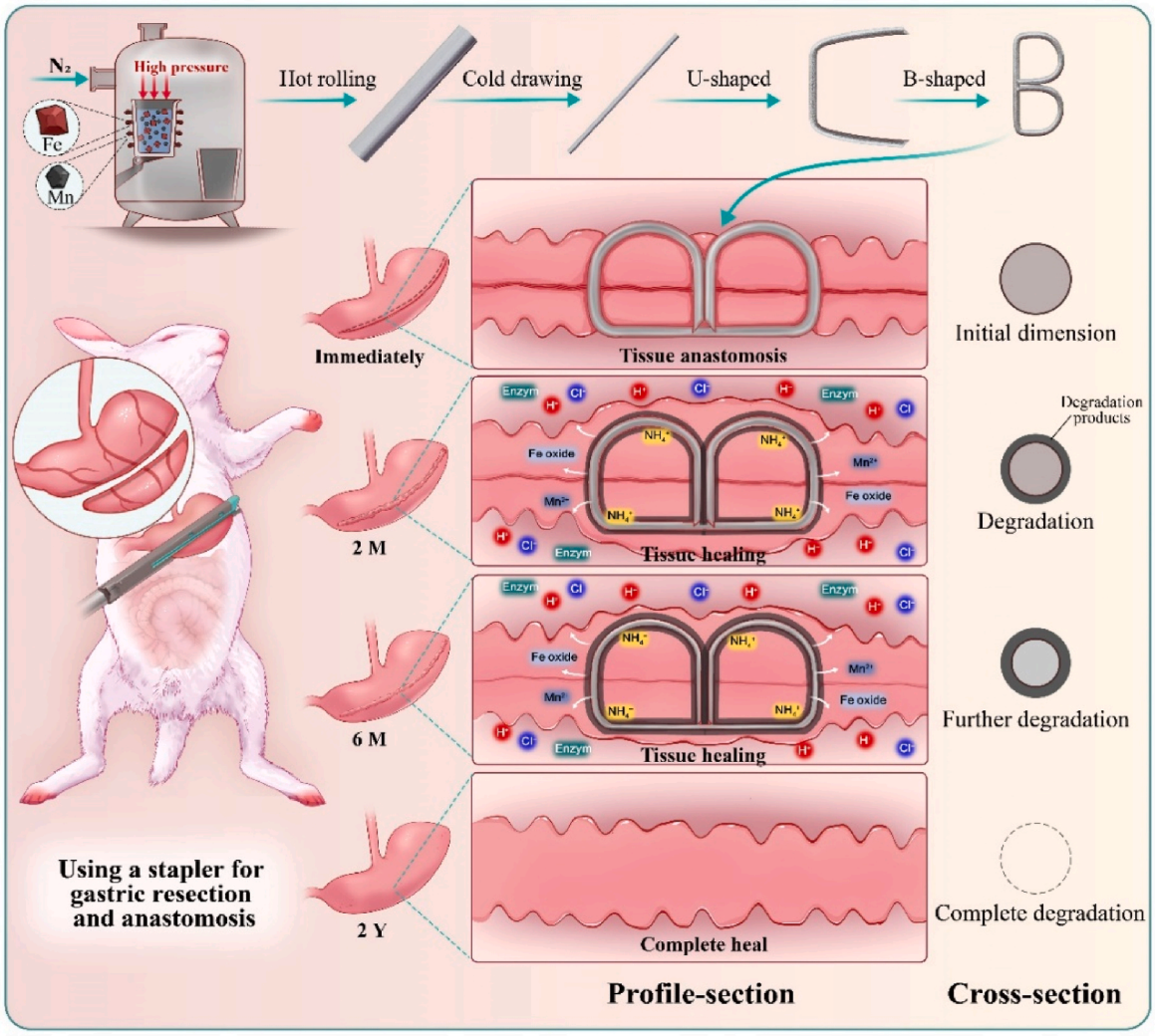

Scheme 1. Summarized diagram for the fabrication, implantation, anastomosis and degradation processes of the HN–Fe staples.

Table 1
Chemical compositions of HN–Fe and Fe wires, wt.%.

HN–Fe wire	Mn	N	C	O	S	P	Si	Fe
	29.32	0.5800	0.0150	0.0096	0.0160	0.0070	<0.1	Bal.
Fe wire	Sn	Cu	C	Sb	As	Bi	Pb	Fe
	0.012	0.009	0.002	0.006	0.006	0.002	0.001	Bal.

2.2. Tensile test

The static uniaxial tensile tests were conducted on a universal tensile machine (Instron-5569) at room temperature for the wires before and after immersion, according to GB/T 228.1–2010 with a strain rate of 6.7 $\times$ 10^{-4} s^{-1} and a gauge length of 25 mm. The immersion parameters were as described in section 2.2.1. After 1, 3, 7, 14, 21 and 28 days of immersion, the specimens were removed from the Hank's solution (Table 2), rinsed with deionized water and anhydrous ethanol, and dried at room temperature. At least three specimens for each set were tested to ensure that the results obtained were reliable.

2.3. Degradation test in vitro

2.3.1. Immersion test

To evaluate the degradation properties of wires, weight loss analysis was used. The wire was cut into the length of 12 mm and each set of immersed specimens consisted of seven. Before immersion, the specimens were weighed and labeled. Based on ASTM-G31-72, the wires were all completely immersed with a ratio of 20 mL/cm^2 at 37 °C in Hank's solution. Changing the solution every two days. Considering that bacteria may affect the corrosion process of Fe alloys, additional antibiotics were added to the solution, including penicillin 100 U/mL and

Table 2
Compositions of Hank's solution, g/L.

NaCl	KCl	KH_2PO_4	$MgSO_4$	$NaHCO_3$	$CaCl_2$	$Na_2HPO_4{\cdot}12H_2O$	Glucose
8.0	0.4	0.06	0.1	0.35	0.185	0.12	1.0

streptomycin 100 μg/mL [28].

For the removal of degradation products, the immersed specimens were removed from the solution at 7, 14, and 28 days and ultrasonically cleaned in an acid wash for 2 min. The specimens were then weighed again. An average result was obtained by measuring at least three specimens for each time. Calculation of the corrosion rate (CR, mm/year) was given by Eq. (1) [25]:

$$CR = (K \times W) / (A \times T \times D) \quad (1)$$

where K is 87,600, W is the weight loss (g), A is the exposed area of the specimen (cm^2), T is the immersion time (h), and D is the density of alloys (g/cm^3).

2.3.2. Electrochemical measurement

The electrochemical measurements were performed on a Gamry Reference 600+ electrochemical workstation by a standard three-electrode system, where the saturated calomel electrode (SCE) was the reference electrode, the platinum electrode was the counter electrode, and the wire was the working electrode. At least three tests were performed on all specimens at 37 °C in Hank's solution. A 1 h open circuit potential (OCP) test was conducted to determine the stability of the electrochemical system.

The potentiodynamic polarization was tested from the corrosion potential (E_{corr}) to the cathode (−0.5 V) and anode (+0.5 V), respectively. The scan rate was 0.33 mV/s. The CR of wire was calculated by Eq. (2):

$$CR = 3.27 \times 10^3 \times I_{corr} \times E_w / \rho \quad (2)$$

where I_{corr} is the corrosion current density, E_w is the weight equivalent, taken as 27.92 g eq^{-1}, and ρ is the density of the wire (g/cm^3).

The electrochemical impedance spectroscopy (EIS) was tested in the frequency range from 100 kHz to 10 mHz. The excitation signal was the sinusoidal voltage with an amplitude of 10 mV. Gamry Echem Analyst software was used to fit and analyze the data.

2.4. Microstructural characterization

X-ray diffraction (XRD, D/max 2400 X) was used to characterize the phase structure of the initial wires with a scanning speed of 10°/min. The radiation source was Cu-Kα with a wavelength of 0.154056 nm.

Scanning electron microscope (SEM, FEI Inspect F50) was used to observe the fracture morphology after tensile test, the surface morphology before degradation, and the corrosion morphology after degradation of the specimens. Energy dispersive spectrometer (EDS) was used to semi-quantitatively analyze the compositions of the wires and their degradation products.

2.5. Degradation test in vivo

Sixteen male New Zealand white rabbits (2.5–3.0 kg) were randomly divided into HN–Fe-linear-cut staple group and Ti-linear-cut staple group, with eight rabbits in each group. The rabbits were anesthetized by an intramuscular injection of ketamine (3.0 mg/kg) and 2 mL 3 % sodium pentobarbital. The animals were placed in supine position, and immobilized. Epigastrium were shaved and sterilized with povidone-iodine. Cut along the linea alba below xiphoid process to expose the left side of the greater curvature. Partial gastrectomy was performed for greater curvature with HN–Fe-linear-cut staple and Ti-linear-cut staple, respectively. Then, returning gastric stump and layer sutured and incision closed. Postoperative intramuscular injection of 8×10^5 U penicillin sodium/each rabbit for three days to prevent infection. Abdominal X-ray fluoroscopy was performed at 1, 2 and 6 months postoperatively to clarify the morphology and degradation of the staples *in vivo*. After the removal of the anastomosis staples, weight loss analysis, surface and cross-section corrosion morphology of the staples were carried out as described in the previous section.

2.6. Biocompatibility test

2.6.1. Histology evaluation

Six months after partial gastrectomy, all experimental animals were euthanized with sodium pentobarbital injection. The gastric wall tissue with staples were embedded by methyl methacrylate, and sliced (50 μm) with a hard tissue microtome (LEICA, Germany). The heart, kidney, liver, lung and spleen were collected and fixed with 10 % formaldehyde solution for 48 h, embedded in paraffin, and cut into sections with a tissue microtome. All samples were stained with hematoxylin-eosin (HE). And then sections were transferred to the two pathologists for pathology evaluation.

2.6.2. Blood routine and biochemistry

After 2 and 6 months, all the experimental animals were anesthetized with 3 % sodium pentobarbital, the blood (2 mL) was drawn from their peripheral ear vein. Routine blood counts and liver and kidney function were examined using the ProCyte Dx and Catalyst One kits (IDEXX, USA).

2.6.3. Reverse transcription-polymerase chain reaction (RT-PCR)

The gastric wall tissue at the insertion of the staples was collected and cleaned with phosphate buffered Saline. Total RNA from 50 mg tissue was isolated using RNAiso Plus (TAKARA Biotechnology, China). The concentration of RNA was determined by spectrophotometry at 260 nm. Total RNA (1 μg) was reverse-transcribed using a PrimeScript RT reagent Kit (Perfect Real Time) (TAKARA Biotechnology, China) in a total volume of 20 μL. Quantitative real-time PCR was performed on cDNA samples using a LightCycler480 II instrument (Roche, Basel, Switzerland) with the SYBR Green Premix Ex Taq II (TAKARA Biotechnology, China) in a total volume of 20 μL. The primer sequences for gastric wall tissues were as follows: IL-10-F, 5′-TTGTTAACCGAGTCCCTGCTT-3′; IL-10-R, 5′- CCACTGCCTTGCTCTTGTTT-3′; TNF-α-F, 5′-ACCCTCAGATCAGCTTCTCG-3′; TNF-α-R, 5′- TTGACCGCTGAAGAGAACCT-3′; TGF-β1-F, 5′-ACGGGCTCAACATCTACACA-3′; TGF-β1-R, 5′-GTGTCCAGGCTCCAGATGTA-3′; IL-8-F, 5′-TACAGAGCTTCGATGCCAGT-3′; IL-8-R, 5′-CCTTCTGCACCCACTTTTCC-3′; and GAPDH-F, 5′-GCTGAACGGGAAACTCACTG-3′; GAPDH-R, 5′-CCGAAGGTAGAGGAGTGGGTG-3′. The expression level of glyceraldehyde-3-phosphate dehydrogenase (GAPDH) was measured and used as an internal control. The data were analyzed using $2^{-\Delta\Delta Ct}$ relative expression quantity as previously described [29].

2.6.4. Enzyme-linked immunosorbent assay (ELISA)

ELISA was used to measure the inflammatory factor secretion of gastric wall tissue at the insertion of the anastomotic nail. The gastric wall tissue was collected and cleaned with phosphate buffered saline, and the tissue were dissected out and homogenized in lysis buffer (tissue weight: lysis solution volume = 1:5). The homogenized samples were centrifuged at 5000 *g* for 10 min, and the supernatants were collected for further analysis. The concentrations of Interleukin 10 (IL-10), Tumor Necrosis Factor Alpha (TNF-α), Transforming Growth Factor Beta 1 (TGF-β1) and Interleukin 8 (IL-8) were determined using a Rabbit Interleukin 10 ELISA Kit (Cloud-Clone Corp., USA), a Rabbit Tumor Necrosis Factor Alpha ELISA Kit (Cloud-Clone Corp., USA), a Rabbit Transforming Growth Factor Beta 1 ELISA Kit (Cloud-Clone Corp., USA), a Rabbit Interleukin 8 ELISA Kit (Cloud-Clone Corp., USA) according to the manufacturers' instructions. The results were reported in picograms per mL of proteins and compiled using Prism 9.0 GraphPad Software (GraphPad Software Inc., San Diego, CA).

3. Results

3.1. Mechanical properties and the attenuation with time after immersion

The phase structure, mechanical properties and their attenuation of the experimental HN–Fe and Fe wires are shown in Fig. 1. Compared to the Fe wire, HN–Fe wire is non-ferromagnetic and mainly consists of austenitic and ε-martensitic phases, showing excellent MRI compatibility (Fig. 1a). The 0.2 % offset yield strength (σ_y), ultimate tensile strength (σ_u) and uniform elongation (ε_u) of HN–Fe wires are 762.8 ± 3.1 MPa, 1023.2 ± 8.1 MPa and 51.0 ± 3.4 %, respectively, which are 1.38, 1.41 and 1.26 times higher than that of Fe wires (Fig. 1b). It is recognized that the mechanical properties of the HN–Fe wire are much higher than the standard regulated by YY 0875–2013, showing that it can provide sufficient mechanical support after anastomosis. The fracture morphologies of both wires exhibit ductile fracture, but there are significant differences (Fig. 2a and b). The dimples with a greater number, smaller size, and more uniform distribution are found in the fracture of HN–Fe wires. Although the reduction of area for Fe wire is apparently higher, the dimples are larger and unevenly distributed, which may be the reason for its lower plasticity.

The mechanical properties of HN–Fe and Fe wires after immersion in Hank's solution for different times are presented in Fig. 1c and d. It can be seen that the mechanical properties of the two wires suffer different degrees of attenuation with the extension of immersion time. Within 7 days of immersion, the attenuation speeds of the σ_y, σ_u and ε_u of HN–Fe wires are slow, but the error ranges in ε_u are large, which may be related to the appearance of local corrosion. However, after 14–28 days of immersion, the attenuation speeds of all three characteristics are obviously accelerated. It suggests that the number and size of corrosion pits may inevitably increase in the late stage of immersion. In contrast, the Fe wire has inferior mechanical properties and, as a pure metal, degrades more slowly, resulting in a lower attenuation speed of its mechanical properties throughout the immersion processes. It is noteworthy that the mechanical properties of the HN–Fe wire are consistently much higher than those of the Fe wire, exhibiting a pronounced mechanical properties advantage.

The fracture morphologies of HN–Fe and Fe wires before and after immersion in Hank's solution for different times are displayed in Fig. 2. The results show that with the extension of immersion time, the mechanical properties of both wires are attenuated, but the fracture type remains as ductile fracture. Compared to the unimmersed results, there is no evident change in the fracture morphologies of the two wires. Meanwhile, a small number of degradation products are observed attaching to the fractures. In addition, numerous corrosion pits are found at the fracture of the HN–Fe wire after 28 days of immersion, and the appearance of these corrosion pits leads to a much faster attenuation speed of its mechanical properties.

3.2. Degradation behaviors in vitro

The electrochemical performances of HN–Fe and Fe wires immersed in Hank's solution are compared in Fig. 3. The corrosion current density (I_{corr}) and corrosion rate (CR) obtained by fitting the potentiodynamic polarization curves (Fig. 3a) are shown in Fig. 3b. The results show that the I_{corr} and CR of the HN–Fe wire are obviously lower than those of the Fe wire. Meanwhile, no passivation behavior is observed on the anodic branches of both wires, indicating that the accumulation of degradation products on the surface of the specimens is not present at this time, and the corrosion is still in the beginning stage.

To investigate the corrosion mechanism of the wires, EIS measurements were performed. In general, the time constant of the electrochemical process is represented by the peak of the -phase angle vs. frequency curves in the Bode plot, so the number of peaks is equal to the number of components in the circuit. Two peaks are clearly observed on the -phase angle vs. frequency curves of both wires (Fig. 3c). Accordingly, a double time constant equivalent circuit is used to fit the EIS results, as shown in Fig. 3d. CPE_1 is the capacitance of the corrosion product layer, CPE_2 is the capacitance of the double electrode layer formed at the interface between the alloy and the electrolyte, R_{cp} is the corrosion product layer resistance, R_{ct} is the charge transfer resistance, and R_s is the solution resistance. The fitting results are summarized in Table 3. The results show that R_{ct} can be used to compare the degradation rates due to the fact that R_{ct} exhibits the greatest difference between the two wires and its value is much larger than R_s and R_{cp}. The HN–Fe wire has a significantly larger R_{ct} value, leading to a more

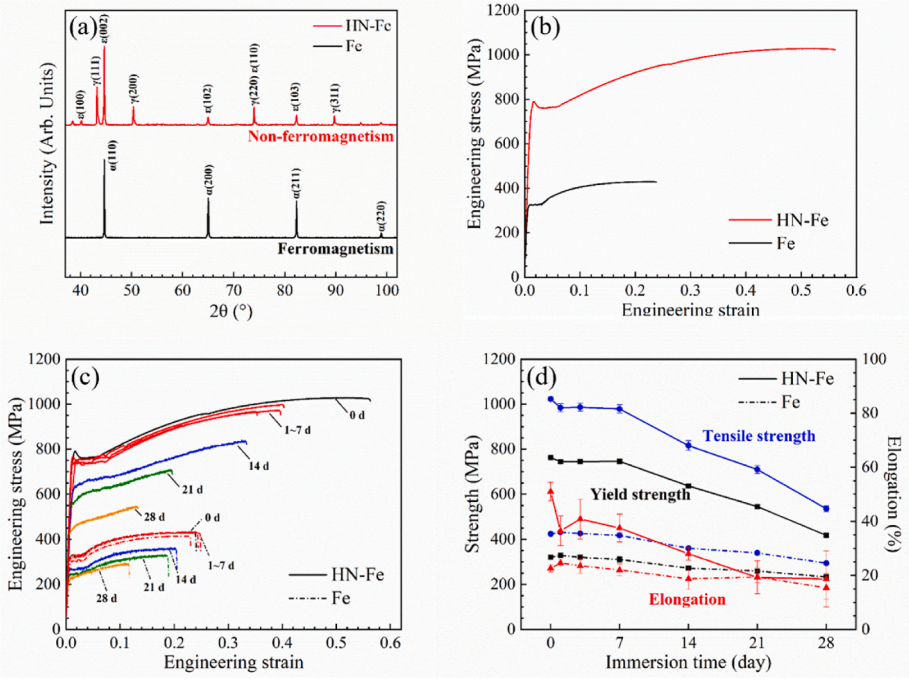

Fig. 1. XRD pattern (a), engineering stress-strain curves (b), the attenuation of mechanical properties with time (c) and (d) of HN–Fe and Fe wires.

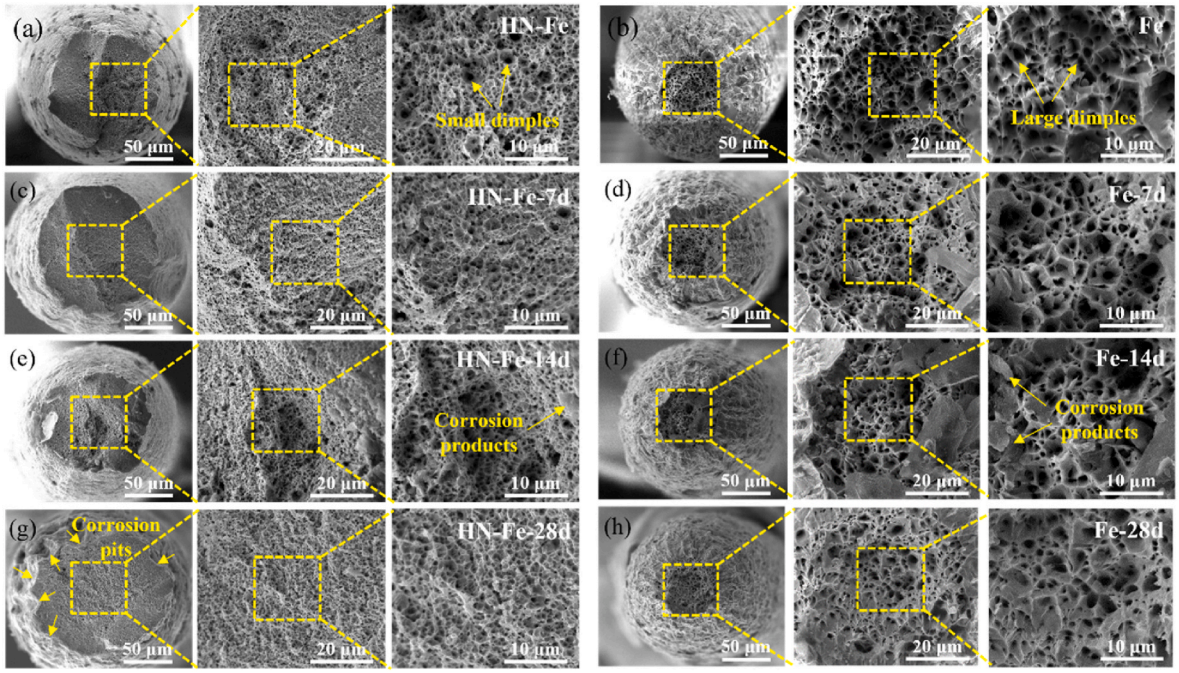

Fig. 2. Fracture morphologies of HN–Fe and Fe wires before and after immersion in Hank's solution for different times: (a, b) 0 d; (c, d) 7 d; (e, f) 14 d; (g, h) 28 d.

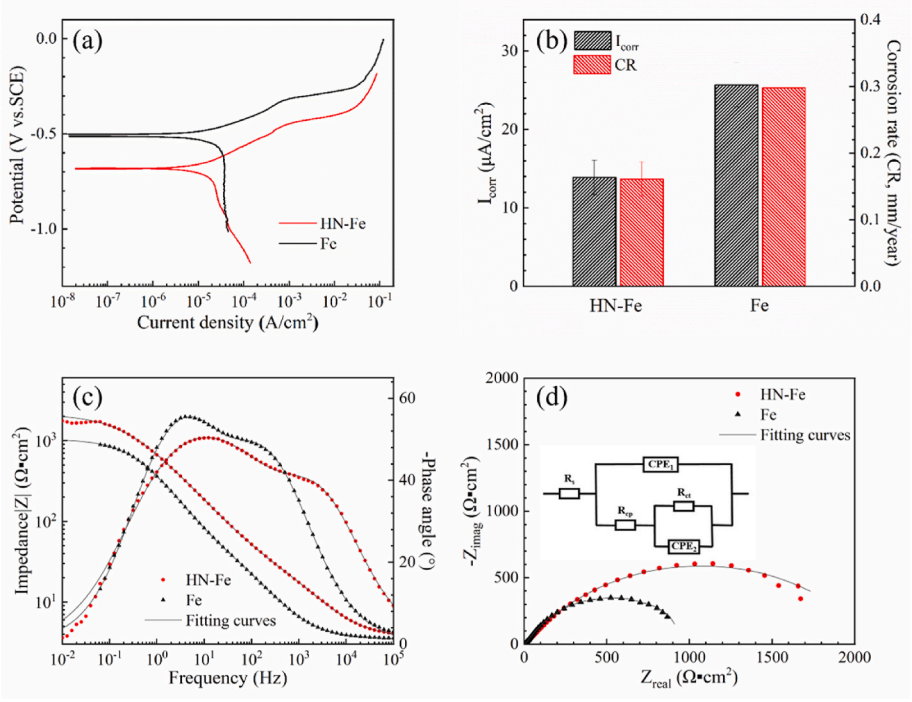

Fig. 3. Electrochemical performances of HN–Fe and Fe wires immersed in Hank's solution: (a) potentiodynamic polarization curves, (b) fitted I_{corr} and corrosion rate, (c) Bode plots, and (d) Nyquist and equivalent circuit plots.

Table 3
Fitting results of EIS measurements for HN–Fe and Fe wires.

	R_s (Ω■cm^2)	R_{cp} (Ω■cm^2)	R_{ct} (kΩ■cm^2)	CPE_1 (μS■s^a/cm^2)	CPE_2 (μS■s^a/cm^2)
HN–Fe	4.1 ± 0.6	44.0 ± 11.5	1.9 ± 0.3	111.5 ± 24.7	219.0 ± 85.7
Fe	4.0 ± 0.5	87.1 ± 26.0	0.6 ± 0.1	222.7 ± 22.8	153.3 ± 54.2

kinetically difficult degradation reaction, which is consistent with the potentiodynamic polarization results. Also, in the Nyquist plot, the HN–Fe wire with lower degradation rate shows a larger curve radius. The electrochemical analysis above characterizes the degradation behavior at the initial stage due to the limited immersion time. Therefore, it can be concluded that the degradation rate of the HN–Fe wire is obviously lower than that of the Fe wire at the initial stage of degradation.

In order to evaluate the long-term degradation behavior, the surface

corrosion morphologies, degradation products and degradation rates of HN–Fe and Fe wires immersed in Hank's solution for different times are presented in Fig. 4. It can be seen that the corrosion degree aggravates with the extension of the immersion time, and the corrosion morphology differs clearly (Fig. 4a–f). A large number of corrosion pits are observed on the HN–Fe wire surface, while the Fe wire surface is characterized by corrosion grooves along the drawing direction, originating from the defects produced during the drawing process. In addition, the two wires exhibit different corrosion morphologies, and the corrosion products of the HN–Fe and Fe wires are pin-like and rod-like, respectively. The corrosion products of both wires contain a large amount of O, Ca and P, where the contents of O and P in HN–Fe can be semi-quantitatively considered to be higher than those in Fe (Fig. 4g and h). Fig. 4i provides the variation trend of the CR with the increase of immersion time. The CRs of two wires decrease with the increase of immersion time. The CR of the HN–Fe wire is higher than that of the Fe wire throughout the degradation process, especially at 7 days of immersion, the CR of HN–Fe wire is about 2.5 times higher than that of Fe wire. However, at the later stage of immersion, the CR of HN–Fe wire is only slightly higher than that of Fe wire, which may be related to the attachment of degradation products on the surface.

In conclusion, compared to the Fe wire, the CR of HN–Fe wire is slower in the initial stage of degradation and obviously accelerated in the late stage of degradation, which is consistent with the variation trend of mechanical property attenuation.

3.3. Degradation behaviors in vivo

The surgical photographs and postoperative anastomosis effects of Ti and HN–Fe staples implanted in animals are shown in Fig. 5. During the partial gastrectomy, Ti-staples and HN–Fe-staples are able to smoothly complete the cutting and suturing process, with neat cutting edges and no leakage of gastric juice, and both staples possess excellent closure performance for blood vessels, with no hemorrhage at the anastomosis (Fig. 5a and b). Abdominal X-ray fluoroscopy is performed immediately after partial gastrectomy, which shows that dense Ti-staples and HN–Fe-staples (Fig. 5c and d). After the implantation for 2 months, both staples represent excellent anastomosis, the local tissue was smooth and dense, and no infection or fistula was found (Fig. 5e and f). Follow-up fluoroscopy is performed after the surgery for 6 months, the results demonstrate that morphology of both staples are normal without discontinue of anastomosis (Fig. 5g and h). In addition, compared to immediately fluoroscopy after the surgery, HN–Fe staples undergo significant degradation and become blurred after the surgery for 6 months. There is significant degradation of the HN–Fe staple section, no significant inflammatory response is found, and tissue growth towards the degradation area is observed, indicating that the HN–Fe staples have excellent biocompatibility. In contrast, the tissue around the Ti staples presents a regular circular cross-section (Fig. 5i and j).

The *in vivo* degradation behavior of HN–Fe staples and the comparison with the *in vitro* results are summarized in Fig. 6. Through corrosion morphology, it is found that the local corrosion occurred on the surface of the HN–Fe staples for 6 months, but the pits uniformly distributed and most of them were shallow. And no fracture happened after the

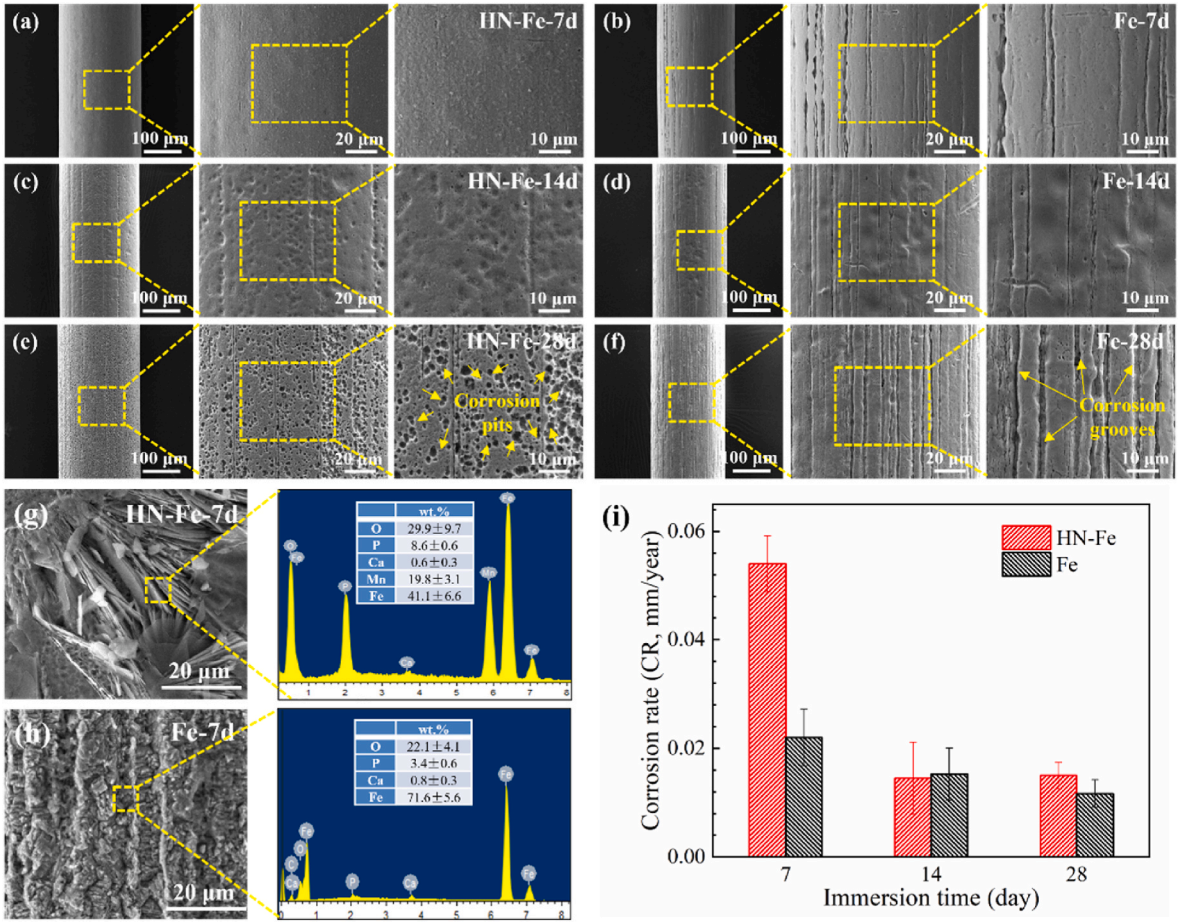

Fig. 4. Surface corrosion morphologies of HN–Fe (a, c, e) and Fe (b, d, f) wires immersed in Hank's solution for different times: (a, b) 7 d; (c, d) 14 d; (e, f) 28 d, pin-like and rod-like corrosion products on the surface of the HN–Fe (g) and Fe (h) wire after 7 days of immersion, respectively, and the variation trend of CR with the increase of immersion time (i).

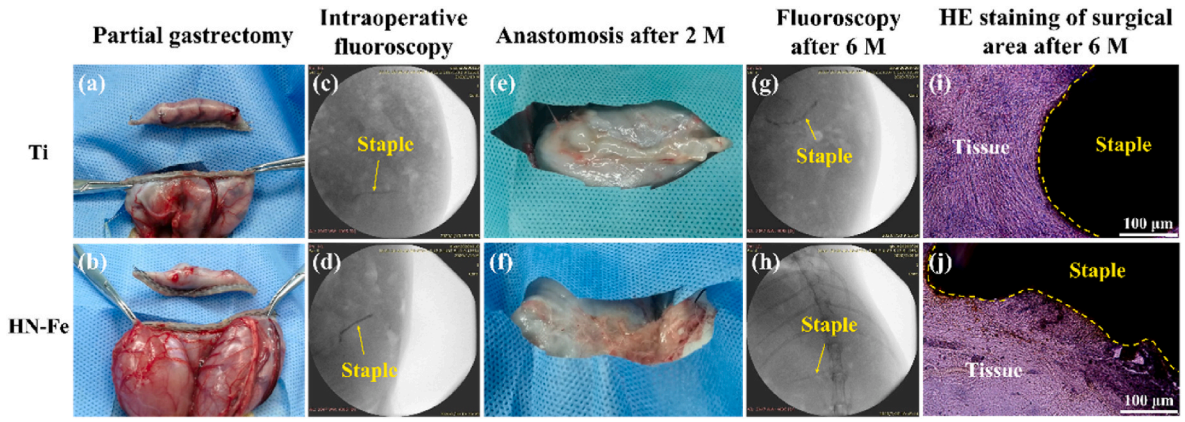

Fig. 5. Partial gastrectomy (a, b), intraoperative abdominal X-ray fluoroscopy (c, d), anastomosis after 2 M (e, f), follow-up fluoroscopy after 6 M (g, h) and HE staining of surgical area after 6 M (i, j) of Ti and HN–Fe staples implanted in animals.

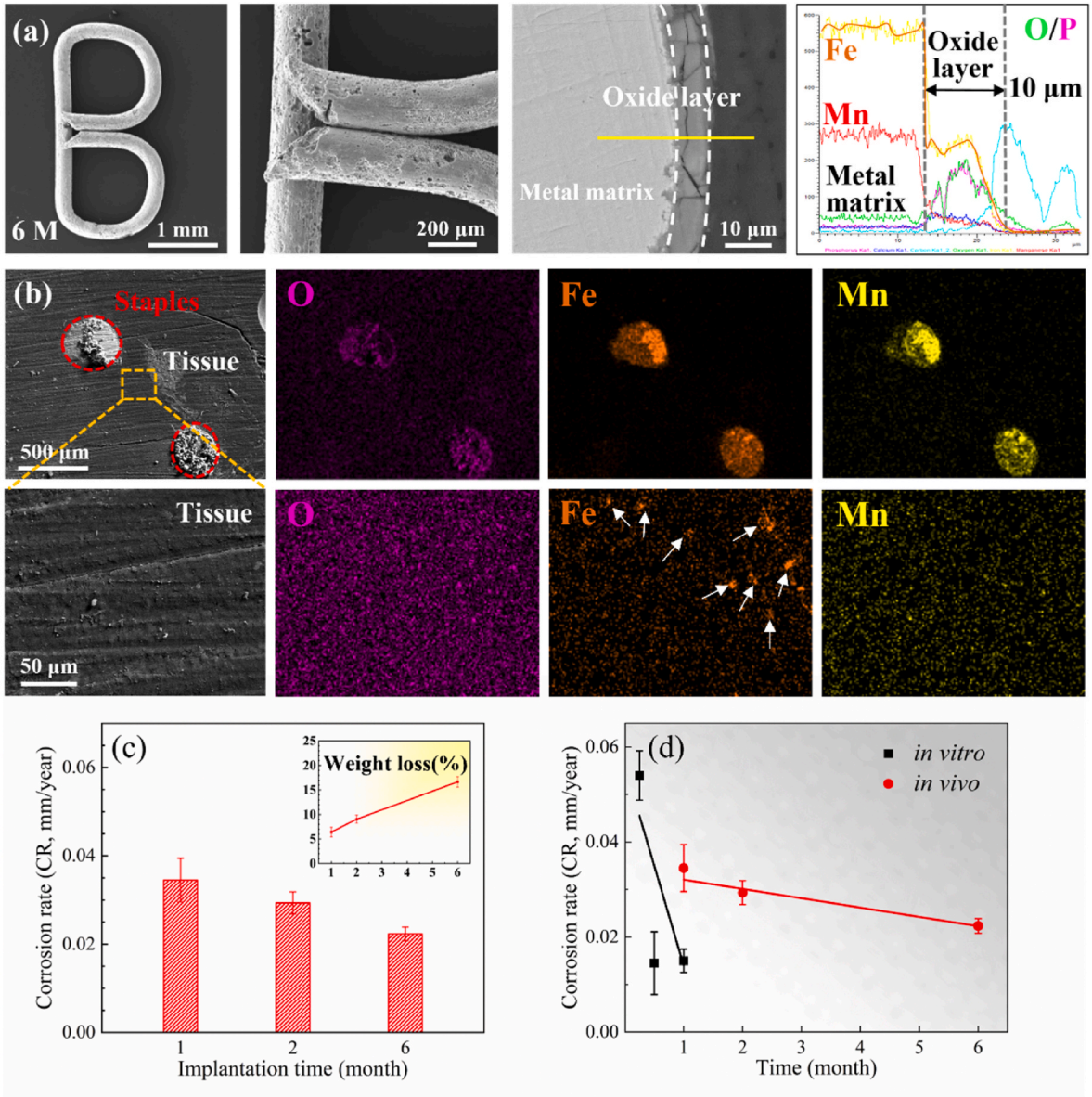

Fig. 6. Corrosion morphologies, cross-sectional corrosion product layers and elemental changes of line scanning (a), element distribution in the surrounding tissue (b) of HN–Fe staples implanted in animals for 6 M, the corresponding corrosion rates including weight loss (c) and the comparison of corrosion rates *in vitro* and *in vivo* (d).

implantation, indicating that they still can provide adequate mechanical performance. From the cross-section results, degradation product layer was very homogeneous, and elements such as Fe, Mn, O, Ca, and P uniformly distributed. The thickness of the degradation product layer, which could obtain by the variation of O and P elemental content, is 10 μm after the implantation for 6 months (Fig. 6a). In addition, the chemical compositions of tissue surrounding the HN–Fe staples were analyzed by EDS mapping. It is found that Fe enriched in block shape without obvious Mn enrichment (Fig. 6b). The CR decreases obviously with the increase of implantation time. It is worth noting that compared to the *in vitro* results, the HN–Fe staple maintains a high corrosion rate and a continuous increase in weight loss at the late stage of implantation, and is expected to be completely degraded in about 2 years (Fig. 6c and d).

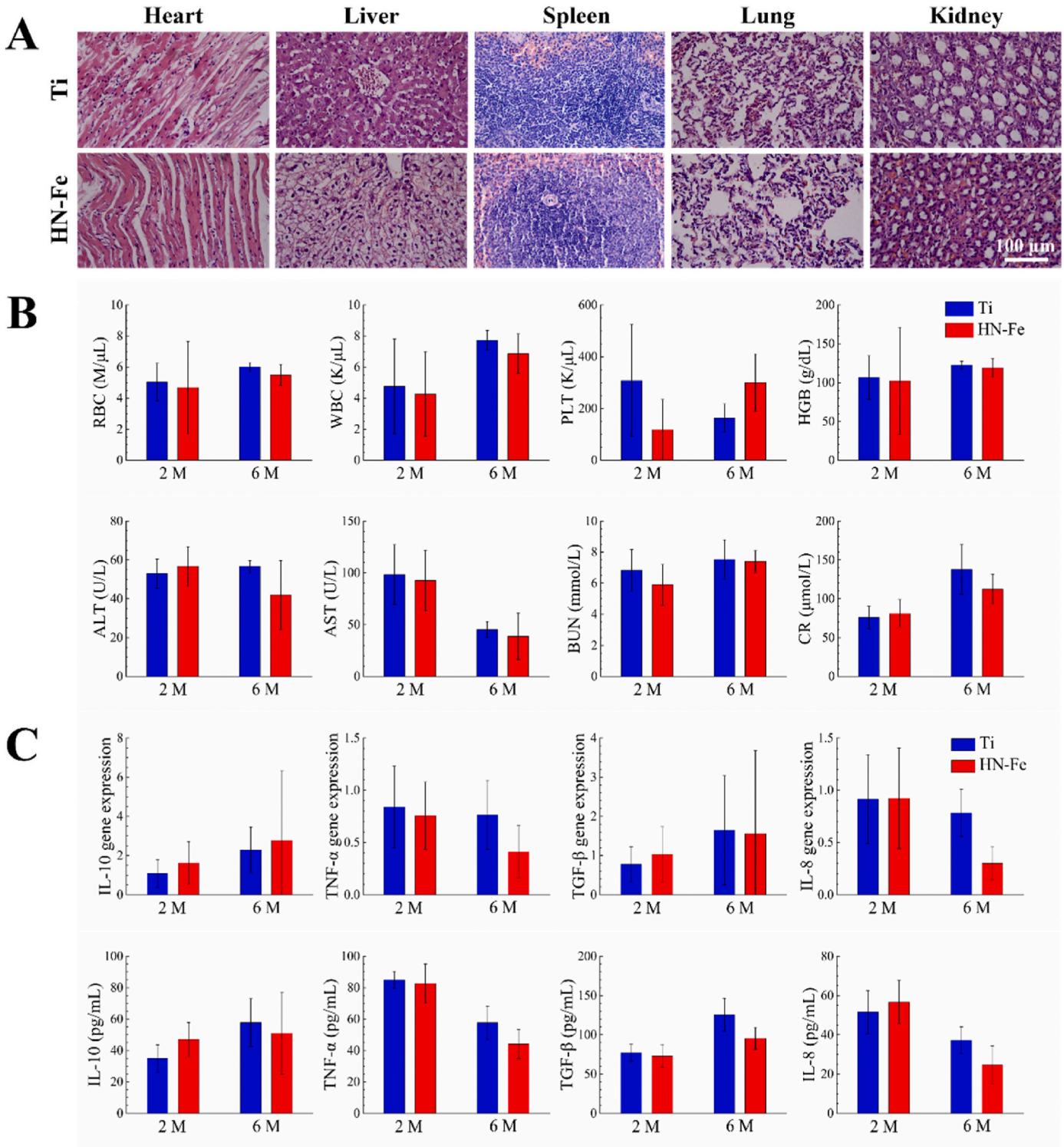

Fig. 7. Biocompatibility evaluation *in vivo*. (A) Histopathological observation of major organ sections after implantation for 6 months; (B) Blood routine and biochemistry and (C) Gene and protein expression of inflammatory factors after implantation for 2 and 6 months of the Ti and HN–Fe staples.

3.4. Biocompatibility evaluation

HE staining of the heart, liver, spleen, lungs, and kidneys does not reveal obvious histomorphological damage on 6 months after partial gastrectomy (Fig. 7A). These data confirm that the HN–Fe staple is safe at the histomorphological level. Furthermore, the detection of blood counts and biochemical parameters is another method for the *in vivo* assessment of safety. As shown in Fig. 7B, red blood cells count (RBC), white blood cells count (WBC), platelet count (PLT), hemoglobin concentration (HGB), alanine aminotransferase (ALT), aspartate transaminase (AST), blood urea nitrogen (BUN) and creatinine (CR) are selected as safety evaluation indicators. There is no significant difference between the HN–Fe staple and Ti staple at 2 and 6 months after partial gastrectomy. To evaluate the inflammatory response related to the implantation of staples, IL-10, TNF-α, TGF-β and IL-8 were selected as Inflammation evaluation indicators. The results of RT-PCR and ELISA show that there is no difference in the expression of inflammatory factor genes and proteins between the two types of staples at 2 and 6 months after implantation (Fig. 7C).

4. Discussion

Compared with manual suture, surgical staples are widely used in gastrointestinal anastomosis as they can effectively shorten surgical time and reduce postoperative complications [30]. Ti alloy staple with sufficient mechanical strength and good biological safety are widely used in clinical practice [31]. The application of biodegradable sutures could fully eliminate the adverse effects of allergic reaction, foreign body reaction and tissue adhesion caused by Ti alloy staple that exist permanently in human body [32]. Hence, it is urgent to develop biodegradable staples with benign biocompatibility and favorable mechanical maintenance. In present study, we fabricated the biodegradable HN–Fe alloy staple with favorable mechanical properties and biocompatibility, to discover its feasibility to apply in gastrointestinal staple (Scheme 1).

4.1. Mechanical properties of HN–Fe staples

At present, biodegradable metal materials have been widely used in the field of cardiovascular applications. Degradable Mg-based and Fe-based vascular stents have been applied in clinical practice [33,34], and biodegradable Zn-based vascular stents have also demonstrated benign safety and biological functions in preclinical studies [35]. However, biodegradable materials used as gastrointestinal staples face more complex and unique mechanical and biological environments. The repeated peristalsis gastrointestinal tract containing multiple digestive fluids have put forward more stringent requirements for the mechanical property of the anastomotic staples [36,37].

Compared with other degradable metal fine wires, degradable Fe and its alloys have unique advantages in strength and elongation. The ultimate tensile strength and elongation of recently developed biodegradable alloy wires are summarized in Fig. 8. The results indicate that HN–Fe wire has obvious advantage in mechanical properties, which is much higher than the other biodegradable metal wires [38–56]. Pure Fe wires exhibited a good strength-plasticity matching [52]. For Fe–N alloy, the strength was significantly increased, but the plasticity was decreased [57]. Although the alloying elements such as Mn and C could improve the mechanical properties of Fe alloys [58], they were prone to precipitate second phases or produce α-martensite transformation during the annealing treatment and large deformation in the drawing process, which restricted their application for wires. For HN–Fe, both the strength and plasticity are much higher than that of all the other degradable metal wires [38–56], and after attenuation with time, the mechanical advantages are still considerable (Fig. 1d). On this basis, HN–Fe alloy with high strength and plasticity provides the possibility of further reducing the size of the staples to shorten the degradation period and reduce the stimulation for the healing tissues.

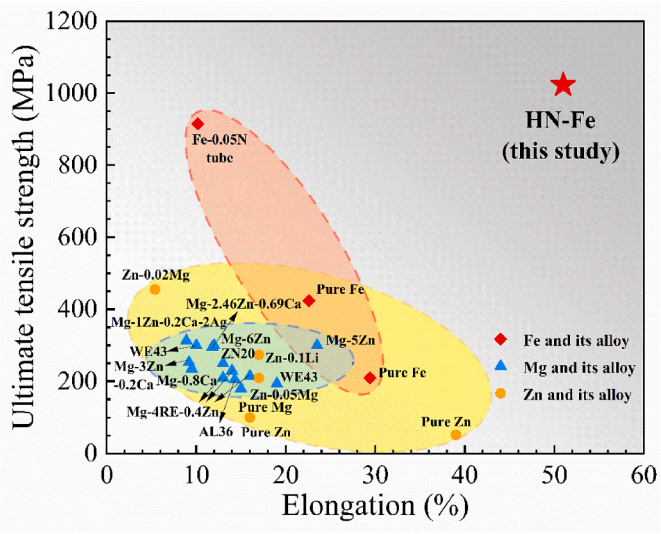

Fig. 8. Ultimate tensile strength and elongation comparison of recently developed biodegradable alloy wires [38–56].

In the *in vivo* experiment, all animals did not show symptoms such as intestinal fistula within 6 months after the implantation of the anastomotic staples, and the anastomotic staples were tightly arranged and had good continuity in abdominal X-ray fluoroscopy (Fig. 5h). When collecting tissue samples, it can be clearly seen that the anastomotic site is well healed, and compared to Ti staples, the tissue proliferation at the implantation site of HN–Fe staples is significantly increased (Fig. 5j). Furthermore, gastrointestinal staplers also play a cutting role in surgery. The results of this study indicate that HN–Fe alloy anastomotic staples could neatly and smoothly cut tissues and stop bleeding even in areas with abundant blood vessels (Fig. 5b), which strongly proves that HN–Fe alloy anastomotic staples have favorable mechanical property.

4.2. Degradation behaviors of HN–Fe staples

The slow degradation rate has become a bottleneck problem that urgently needs to be solved for biodegradable Fe alloys [59]. In recent years, increasing efforts have been paid to improve the degradation rate of Fe alloys. Hermawan et al. first explored the feasibility of preparing biodegradable Fe alloys through Mn alloying [60]. In addition to enhancing the mechanical properties, the addition of Mn also reduced the standard electrode potential of Fe alloys, significantly improving their degradation rate compared to pure Fe [61]. Thus, Mn is currently considered the preferred alloying element for biodegradable Fe alloys. Based on this, alloying elements such as C [19], Si [20], Pd [21] and Ag [22] were used to further increase the degradation rate of Fe alloys. However, due to the precipitation of second phase and the large deformation, local corrosion was generally aggravated as well. At present, biodegradable Fe–N alloy stents have entered the clinical trial stage, which have solved the key problem of slow degradation rate of Fe alloys and are expected to completely degrade within two years of implantation [62]. However, due to the low solubility of N element in Fe, Fe–N alloys are still ferromagnetic, resulting in poor MRI compatibility. Also, accelerating corrosion through the precipitation of nitrides has the risk to cause aggravation of localized corrosion, which threatens the life of the patient.

Actually, high-N alloying has been widely used to improve the pitting resistance of stainless steels [63]. Based on these, we firstly developed a biodegradable high-N austenitic alloy in the previous study. It was surprisingly found that by high-N alloying, simultaneous improvement of degradation rate and local corrosion resistance was realized. In this study, the degradation behavior of the HN–Fe wire was consistent with that of the bulk material. A large number of small-sized

and uniformly distributed corrosion pits on the surface of the HN–Fe wires were observed after the immersion experiments *in vitro*, different from the corrosion grooves of Fe wires (Fig. 4e and f). This may be related to the presence of [FeN] clusters evidenced in our previous research, which perform a non-redox reaction with H_2O to increase the degradation rate, and the formation of NH_3, which consumes H^+ to form NH_4^+ to inhibit localized corrosion. The reaction formulas are as follows [25]:

$$2[FeN] + 3H_2O \rightarrow Fe_2O_3 + 2NH_3 \quad (3)$$

$$NH_3 + H^+ \rightarrow NH_4^+ \quad (4)$$

In *in vivo* experimental, abdominal X-ray fluoroscopy indicated that the HN–Fe alloy staples became blurry but tightly arranged without any detachment at 6 months after surgery, which means HN–Fe staples degraded uniformly while ensuring sufficient mechanical strength (Fig. 5h). Previous studies indicated that partial detachment of the anastomotic staples did not affect the healing of anastomotic site, and could also promote the overall degradation rate of the anastomotic staples [13]. However, there are potential safety hazards associated with uncontrollable and unpredictable detachment of the anastomotic nail in clinical practice.

In addition, there were a large number of tissues growing towards the degradation area of the HN–Fe staples, in which cells containing yellow particles can be seen (Fig. 5j). It is considered that macrophages are phagocytic degradation products, which have been observed in the tissues surrounding the staples, mainly solid degradation products of Fe (Fig. 6b), and this degradation process is basically consistent with previous study [23]. The nutritional status of patients has a direct impact on wound healing, and besides protein and amino acids, balanced intake of mineral elements is equally important for wound healing [64]. Fe is one of the key elements in tissue repair after injury, which can promote the tissue repair [64,65]. Therefore, the iron ions released by the degradation of the HN–Fe staples may promote the healing of anastomotic site. In addition, as one of the degradation products, the metabolic process of Mn should theoretically be similar to that of Fe *in vivo*, but further exploration is needed. And the enzymes involved in the synthesis of Mn had a certain inhibitory effect on ROS, which is helpful in reducing the inflammatory response after the implantation of staples [66]. It is worth noting that, unlike *in vitro* degradation, the HN–Fe staples could still maintain a high degradation rate in the later stage of implantation, and weight loss continues to increase (Fig. 6c and d). It is expected to be completely degraded in about 2 years. This degradation period is acceptable for staples.

4.3. Biocompatibility of HN–Fe staples

Biosafety is crucial for medical implants, especially metal implants. Both Fe and Mn are essential trace elements for the human body. The body's Fe is in a dynamic balance of continuous absorption, utilization, storage, and circulation, that is iron homeostasis [67]. Mn is mainly distributed in various tissues and body fluids, as well as in organs such as bone, liver, pancreas and kidney. The daily intake of Fe and Mn element for a healthy adult is 10–15 and 2–5 mg, respectively. Each staple is about 3 mg, and a resection site anastomosis requires about 40 staples (Fig. 5b), totaling about 120 mg of metal. Considering the degradation process, the total amount of metal released from the implanted staples was 0.16 mg/day, which is much less than the Fe intake of 10–15 mg per day. In addition, previous studies have shown that Fe–30Mn (wt.%) alloy could meet the requirements of biological evaluation standards for medical devices (ISO 10993-5) [68]. Therefore, the HN–Fe staples are safe for the human body.

Due to the slow degradation rate of Fe alloys in the early research, Mg alloys and Zn alloys with faster degradation rates have become important materials for developing the degradable anastomotic staples [65]. Nevertheless, the high degradation rate of Mg alloys and the need to improve the strength of Zn alloys still require more explorations for the biodegradable staples by now [69]. Based on the fruitful achievements of biodegradable nitrogen-containing Fe alloys in the cardiovascular field [68], this study firstly evaluated the biocompatibility, degradation and biofunctions of the HN–Fe staples *in vivo*. Moreover, compared with other implantation sites, corrosions caused by digestive fluid and repeated intestinal peristalsis make the environment where the anastomotic staples are located more complex, which might accelerate the corrosion rates of staples [70]. However, the stable degradation characteristics of HN–Fe can avoid the side effects of early rapid degradation caused by corrosion and friction.

Gastrointestinal tract has amazing healing ability and the related studies have shown that the muscle layer fusion occurred 6 days after intestinal anastomosis, and the anastomosis site had a certain mechanical strength after 7 days [71,72], thereby the anastomotic staples would quickly be wrapped around the gastrointestinal tissue to avoid toxic reactions induced by sudden release of metal ions. In addition, Zheng et al. conducted thorough research on the Fe metabolism pathways of biodegradable intravascular Fe stents, and the result showed that a small amount of soluble iron ions entered the bloodstream, but the majority of the solid iron corrosion products were consumed by inflammatory cells such as neutrophils or macrophages. These cells then transported the iron to hemosiderin in adventitia, the lymphatic system, and ultimately the spleen through the circulatory system [23]. Elucidating the iron metabolism pathway *in vivo* will provide strong evidence for the biosafety of biodegradable Fe alloys and greatly promote the research of HN–Fe for medical applications.

Similar to the previous research findings [59], from the H&E-stained images of heart, liver, spleen, lung and kidney of these two staple groups at 6 months post-implantation, no histopathological changes and accumulation of degradation products were found (Fig. 7A). However, the accumulation of solid Fe degradation products was observed in the tissue surrounding the implanted anastomotic staples, without the accumulation of solid Mn degradation products (Fig. 6b). Moreover, there was neglectable change in level of blood routine and biochemistry between two staple groups at 2 months and 6 months (Fig. 7B).

Inflammation of the anastomotic site caused by staples often leads to abdominal pain, vomiting, and even gastrointestinal obstruction, seriously affecting the postoperative recovery of patients [73]. Furthermore, we evaluate the inflammatory response related to the implantation of staples in this study, the result showed that there was no difference in the expression of inflammatory factor genes and proteins between the two types of staples at 2 and 6 months after implantation (Fig. 7C). Therefore, HN–Fe alloy staple demonstrated benign biocompatibility.

4.4. Outlook of this research

Until now, except for Fe–N alloy with nitride precipitates, there is first evidence published that Fe alloys could maintain high degradation rate *in vivo*. In the previous *in vivo* researches, almost no degradation happened for Fe alloys in the later stage of implantation. Thus, this research proved that the Fe alloys without precipitates could be an excellent degradable material for implant applications. With better mechanical performance, degradation behavior and no ferromagnetism, HN–Fe could be used for biodegradable gastrointestinal anastomosis staples, artery stents, etc.

Nevertheless, in this study, *in vitro* degradation rate of the HN–Fe alloy is significantly lower than that *in vivo*, making it difficult to predict *in vivo* results with *in vitro* results (Fig. 6d). Therefore, it remains to be further explored the main factors influencing the difference in degradation behaviors. Additionally, HN–Fe staples were implanted *in vivo* for a relatively short period, and subsequent extension of the implantation period until complete degradation of the staples and larger animal experiments are necessary. The mechanical properties of the HN–Fe wire are much higher than clinical standards, and attempts can be made to

design finer anastomotic staples in the future.

5. Conclusions

In this study, we developed a novel kind of biodegradable high-N Fe alloy wires, which were made into the staples for gastrointestinal anastomosis, and evaluated them *in vivo* and *in vitro*. The conclusions were obtained as follows.

1. The strength and plasticity of HN–Fe wires are much higher than those of the other biodegradable metal wires, and the strength after 28 days immersion is still not less than 240 MPa, meeting the clinical requirements.
2. HN–Fe staples degrade uniformly and maintain a much higher degradation rate *in vivo* compared to *in vitro* in the late stage, which are expected to be completely degraded in about 2 years.
3. HN–Fe staples exhibit excellent biosafety and biocompatibility. After the implantation of 6 months, no histopathological change, abnormal blood routine and biochemistry, and inflammatory reaction occurred.

Ethics approval and consent to participate

In this study, animal experiments of the implantation of staples were authorized by the Ethics Committee of China Medical University (CMUXN2022901).

CRediT authorship contribution statement

Sihan Lu: Writing – review & editing, Writing – original draft, Validation, Software, Methodology, Formal analysis, Data curation, Conceptualization. **Peng Wang:** Writing – review & editing, Writing – original draft, Methodology, Investigation, Data curation. **Qingchuan Wang:** Writing – review & editing, Supervision, Project administration, Funding acquisition, Conceptualization. **Peng Deng:** Methodology, Investigation. **Yonghui Yuan:** Funding acquisition, Writing – review & editing. **Xiaoqing Fu:** Validation, Methodology. **Yinghui Yang:** Supervision. **Lili Tan:** Supervision, Investigation, Funding acquisition. **Ke Yang:** Supervision, Investigation. **Xun Qi:** Writing – review & editing, Visualization, Supervision, Funding acquisition, Conceptualization.

Declaration of competing interest

The authors declare the following personal relationships which may be considered as potential competing interests: Yinghui Yang is currently employed by Silvan Medical Device Co., Ltd.

Acknowledgement

The authors acknowledge financial support from National Natural Science Foundation of China (No. 82272099, 51971222 and 51801220), Construction Project of Liaoning Medical Imaging and Interventional Medical Engineering Research Center (Grant No. 18-006-9-01), STS program (No.20201600200042), DongGuan Innovative Research Team Program (2020607134012) and Basic Applied Research Program of Liaoning Province of China (No. 2022020347-JH2/1013, 2023JH26/103000016).

Appendix A. Supplementary data

Supplementary data to this article can be found online at https://doi.org/10.1016/j.bioactmat.2024.06.005.

References

[1] J. Huang, D.E. Lucero-Prisno 3rd, L. Zhang, W. Xu, S.H. Wong, S.C. Ng, M.C. S. Wong, Updated epidemiology of gastrointestinal cancers in East Asia, Nat. Rev. Gastroenterol. Hepatol. 20 (5) (2023) 271–287.
[2] R. Hajjar, E. Gonzalez, G. Fragoso, M. Oliero, A.A. Alaoui, A. Calvé, H. Vennin Rendos, S. Djediai, T. Cuisiniere, P. Laplante, C. Gerkins, A.S. Ajayi, K. Diop, N. Taleb, S. Thérien, F. Schampaert, H. Alratrout, F. Dagbert, R. Loungnarath, H. Sebajang, F. Schwenter, R. Wassef, R. Ratelle, E. Debroux, J.F. Cailhier, B. Routy, B. Annabi, N.J.B. Brereton, C. Richard, M.M. Santos, Gut microbiota influence anastomotic healing in colorectal cancer surgery through modulation of mucosal proinflammatory cytokines, Gut 72 (6) (2023) 1143–1154.
[3] G. Luglio, F. Corcione, Stapled versus handsewn methods for ileocolic anastomoses, Tech. Coloproctol. 23 (11) (2019) 1093–1095.
[4] G. Vijgen, Surgical stapler, Br. J. Surg. 110 (9) (2023) 1125–1127.
[5] A. Shatkin-Margolis, M. Merchant, R.U. Margulies, O. Ramm, Titanium surgical tacks: are they safe? Do they work?, Female Pelvic Med. Reconstr, Surgery (St Louis) 23 (1) (2017) 36–38.
[6] Y. Zhang, J. Cao, M. Lu, Y. Shao, K. Jiang, X. Yang, X. Xiong, S. Wang, C. Chu, F. Xue, Y. Ye, J. Bai, A biodegradable magnesium surgical staple for colonic anastomosis: *in vitro* and *in vivo* evaluation, Bioact. Mater. 22 (2023) 225–238.
[7] M. Zheng, X. Wang, Y. Chen, O. Yue, Z. Bai, B. Cui, H. Jiang, X. Liu, A review of recent progress on collagen-based biomaterials, Adv. Healthcare Mater. 12 (16) (2023) e2202042.
[8] A. Saad, T. Nunez-Villaveiran, M. Saad, Commentary on: restoration liposuction of the abdomen: high-definition liposuction with umbilicus and lower abdomen improvement using polydioxanone threads, Aesthetic Surg. J. 43 (6) (2023) 424–426.
[9] E. Pesaranhajiabbas, M. Misra, A.K. Mohanty, Recent progress on biodegradable polylactic acid based blends and their biocomposites: a comprehensive review, Int. J. Biol. Macromol. 253 (Pt 1) (2023) 126231.
[10] J. Fu, Y. Su, Y.X. Qin, Y. Zheng, Y. Wang, D. Zhu, Evolution of metallic cardiovascular stent materials: a comparative study among stainless steel, magnesium and zinc, Biomaterials 230 (2020) 119641.
[11] A.A. Oliver, M. Sikora-Jasinska, A.G. Demir, R.J. Guillory 2nd, Recent advances and directions in the development of bioresorbable metallic cardiovascular stents: insights from recent human and *in vivo* studies, Acta Biomater. 127 (2021) 1–23.
[12] V.P.M. Rabeeh, T. Hanas, Progress in manufacturing and processing of degradable Fe-based implants: a review, Prog. Biomater. 11 (2) (2022) 163–191.
[13] H. Guo, J. Hu, Z. Shen, D. Du, Y. Zheng, J. Peng, *In vitro* and *in vivo* studies of biodegradable Zn-Li-Mn alloy staples designed for gastrointestinal anastomosis, Acta Biomater. 121 (2021) 713–723.
[14] H. Wu, C. Zhao, J. Ni, S. Zhang, J. Liu, J. Yan, Y. Chen, X. Zhang, Research of a novel biodegradable surgical staple made of high purity magnesium, Bioact. Mater. 1 (2) (2016) 122–126.
[15] J. Cao, K.W. Jiang, X.D. Yang, Z.L. Shen, P. Guo, Y.C. Yan, Y.C. Cui, L. Han, Y. Lv, Y.J. Ye, S. Wang, Animal experimental study of biodegradable magnesium alloy stapler for gastrointestinal anastomosis, Chin. J. Gastrointest. Surg. 16 (8) (2013) 772–776.
[16] Y. Liu, Y.F. Zheng, X.H. Chen, J.A. Yang, H.B. Pan, D.F. Chen, L.N. Wang, J. L. Zhang, D.H. Zhu, S.L. Wu, K.W.K. Yeung, R.C. Zeng, Y. Han, S.K. Guan, Fundamental theory of biodegradable metals-definition, criteria, and design, Adv. Funct. Mater. 29 (18) (2019).
[17] M.K. Marrache, M.I. Itani, J. Farha, L. Fayad, S.L. Sharara, A.N. Kalloo, M. A. Khashab, V. Kumbhari, Endoscopic gastrointestinal anastomosis: a review of established techniques, Gastrointest. Endosc. 93 (1) (2021) 34–46.
[18] M. Peuster, P. Wohlsein, M. Brügmann, M. Ehlerding, K. Seidler, C. Fink, H. Brauer, A. Fischer, G. Hausdorf, A novel approach to temporary stenting: degradable cardiovascular stents produced from corrodible metal-results 6-18 months after implantation into New Zealand white rabbits, Heart 86 (5) (2001) 563–569.
[19] M. Schinhammer, P. Steiger, F. Moszner, J.F. Löffler, P.J. Uggowitzer, Degradation performance of biodegradable FeMnC(Pd) alloys, Mater. Sci. Eng. C 33 (4) (2013) 1882–1893.
[20] B. Liu, Y.F. Zheng, L. Ruan, *In vitro* investigation of Fe30Mn6Si shape memory alloy as potential biodegradable metallic material, Mater. Lett. 65 (3) (2011) 540–543.
[21] T. Kraus, F. Moszner, S. Fischerauer, M. Fiedler, E. Martinelli, J. Eichler, F. Witte, E. Willbold, M. Schinhammer, M. Meischel, P.J. Uggowitzer, J.F. Löffler, A. Weinberg, Biodegradable Fe-based alloys for use in osteosynthesis: outcome of an *in vivo* study after 52 weeks, Acta Biomater. 10 (7) (2014) 3346–3353.
[22] P. Sotoudehbagha, S. Sheibani, M. Khakbiz, S. Ebrahimi-Barough, H. Hermawan, Novel antibacterial biodegradable Fe-Mn-Ag alloys produced by mechanical alloying, Mater. Sci. Eng. C 88 (2018) 88–94.
[23] J.F. Zheng, Z.W. Xi, Y. Li, J.N. Li, H. Qiu, X.Y. Hu, T. Luo, C. Wu, X. Wang, L. F. Song, L. Li, H.P. Qi, G. Zhang, L. Qin, W.Q. Zhang, X.L. Shi, S.H. Wang, D. Y. Zhang, B. Xu, R.L. Gao, Long-term safety and absorption assessment of a novel bioresorbable nitrided iron scaffold in porcine coronary artery, Bioact. Mater. 17 (2022) 496–505.
[24] J.F. Zheng, H. Qiu, Y. Tian, X.Y. Hu, T. Luo, C. Wu, Y. Tian, Y. Tang, L.F. Song, L. Li, L. Xu, B. Xu, R.L. Gao, Preclinical evaluation of a novel sirolimus-eluting iron bioresorbable coronary scaffold in porcine coronary artery at 6 months, JACC Cardiovasc. Interv. 12 (3) (2019) 245–255.
[25] S. Lu, Q. Wang, Y. Zhang, H. Li, H. Feng, L. Tan, K. Yang, A novel biodegradable high nitrogen iron alloy with simultaneous enhancement of corrosion rate and local corrosion resistance, J. Mater. Sci. Technol. 152 (2023) 94–99.
[26] A. Kastrati, J. Mehilli, J. Dirschinger, F. Dotzer, H. Schühlen, F.J. Neumann, M. Fleckenstein, C. Pfafferott, M. Seyfarth, A. Schömig, Intracoronary stenting and

angiographic results: strut thickness effect on restenosis outcome (ISAR-STEREO) trial, Circulation 103 (23) (2001) 2816–2821.
[27] J.ü. Pache, A. Kastrati, J. Mehilli, H. Schühlen, F. Dotzer, J.ö. Hausleiter, M. Fleckenstein, F.-J. Neumann, U. Sattelberger, C. Schmitt, M. Müller, J. Dirschinger, A. Schömig, Intracoronary stenting and angiographic results: strut thickness effect on restenosis outcome (ISAR-STEREO-2) trial, J. Am. Coll. Cardiol. 41 (8) (2003) 1283–1288.
[28] B. Liu, Y.F. Zheng, Effects of alloying elements (Mn, Co, Al, W, Sn, B, C and S) on biodegradability and *in vitro* biocompatibility of pure iron, Acta Biomater. 7 (3) (2011) 1407–1420.
[29] X. Qi, Y. Okamoto, T. Murakawa, F. Wang, O. Oyama, R. Ohkawa, K. Yoshioka, W. Du, N. Sugimoto, Y. Yatomi, N. Takuwa, Y. Takuwa, Sustained delivery of sphingosine-1-phosphate using poly(lactic-co-glycolic acid)-based microparticles stimulates Akt/ERK-eNOS mediated angiogenesis and vascular maturation restoring blood flow in ischemic limbs of mice, Eur. J. Pharmacol. 634 (1–3) (2010) 121–131.
[30] J.C. Alverdy, Biologically inspired gastrointestinal stapler design: "Getting to Zero" complications, Am. J. Surg. 226 (1) (2023) 48–52.
[31] N.N. Li, W.T. Zhao, X.T. Wu, Can a nickel-titanium memory-shape device serve as a substitute for the stapler in gastrointestinal anastomosis? A systematic review and meta-analysis, J. Surg. Res. 201 (1) (2016) 82–93.
[32] J. Yan, Y. Chen, Q. Yuan, X. Wang, S. Yu, W. Qiu, Z. Wang, K. Ai, X. Zhang, S. Zhang, C. Zhao, Q. Zheng, Comparison of the effects of Mg-6Zn and Ti-3Al-2.5V alloys on TGF-β/TNF-α/VEGF/b-FGF in the healing of the intestinal tract *in vivo*, Biomed. Mater. 9 (2) (2014) 025011.
[33] R.L. Gao, B. Xu, Z. Sun, C. Guan, L. Song, L. Gao, C. Li, J. Cui, Y. Zhang, K. Dou, J. Chen, C. Mu, H. Liu, A. Li, Z. Li, L. Xie, Y. Yang, S. Qiao, Y. Wu, G.W. Stone, First-in-human evaluation of a novel ultrathin sirolimus-eluting iron bioresorbable scaffold: 3-year outcomes of the IBS-FIM trial, EuroIntervention 19 (3) (2023) 222–231.
[34] A. Hideo-Kajita, H.M. Garcia-Garcia, P. Kolm, V. Azizi, Y. Ozaki, K. Dan, H. Ince, S. Kische, A. Abizaid, R. Töelg, P.A. Lemos, N.M. Van Mieghem, S. Verheye, C. von Birgelen, E.H. Christiansen, W. Wijns, T. Lefèvre, S. Windecker, R. Waksman, M. Haude, Comparison of clinical outcomes between Magmaris and Orsiro drug eluting stent at 12 months: pooled patient level analysis from BIOSOLVE II-III and BIOFLOW II trials, Int. J. Cardiol. 300 (2020) 60–65.
[35] H. Yang, D. Jin, J. Rao, J. Shi, G. Li, C. Wang, K. Yan, J. Bai, G. Bao, M. Yin, Y. Zheng, Lithium-induced optimization mechanism for an ultrathin-strut biodegradable Zn-based vascular scaffold, Adv. Mater. 35 (19) (2023) e2301074.
[36] L.Y. Han, X. Li, F. Xue, C.L. Chu, J. Bai, Biocorrosion behavior of micro-arc-oxidized AZ31 magnesium alloy in different simulated dynamic physiological environments, Surf. Coating. Technol. 361 (2019) 240–248.
[37] L.Y. Han, Z.W. Zhang, J.W. Dai, X. Li, J. Bai, Z.H. Huang, C. Guo, F. Xue, C.L. Chu, The influence of alternating cyclic dynamic loads with different low frequencies on the bio-corrosion behaviors of AZ31B magnesium alloy *in vitro*, Bioact. Mater. 7 (2022) 263–274.
[38] J. Bai, L. Yin, Y. Lu, Y. Gan, F. Xue, C. Chu, J. Yan, K. Yan, X. Wan, Z. Tang, Preparation, microstructure and degradation performance of biomedical magnesium alloy fine wires, Prog. Nat. Sci.-Mater. 24 (5) (2014) 523–530.
[39] M. Zheng, G. Xu, D. Liu, Y. Zhao, B. Ning, M. Chen, Study on the microstructure, mechanical properties and corrosion behavior of Mg-Zn-Ca alloy wire for biomaterial application, J. Mater. Eng. Perform. 27 (4) (2018) 1837–1846.
[40] K. Yan, J. Sun, J. Bai, H. Liu, X. Huang, Z. Jin, Y. Wu, Preparation of a high strength and high ductility Mg-6Zn alloy wire by combination of ECAP and hot drawing, Mater. Sci. Eng. 739 (2019) 513–518.
[41] J. Meng, L. Sun, Y. Zhang, F. Xue, C. Chu, J. Bai, Evolution of recrystallized grain and texture of cold-drawn pure Mg wire and their effect on mechanical properties, Materials 13 (2) (2020) 427–437.
[42] Y.-z. Ma, D.-x. Wang, H.-x. Li, C.-l. Yang, F.-s. Yuan, J.-s. Zhang, Microstructure, mechanical properties and corrosion behavior of quaternary Mg-1Zn-0.2Ca-xAg alloy wires applied as degradable anastomotic nails, T. Nonferr. Metal. Soc. 31 (1) (2021) 111–124.
[43] D. Mei, C. Wang, M. Nienaber, M. Pacheco, A. Barros, S. Neves, R.L. Reis, S. Zhu, J. Bohlen, D. Letzig, S. Guan, M.L. Zheludkevich, S.V. Lamaka, Corrosion behavior of Mg wires for ureteral stent in artificial urine solution, Corrosion Sci. 189 (2021) 109567.
[44] H. Zhang, Y. Ding, R. Li, Y. Shen, J. Lei, Achieving exceptional improvement of yield strength in Mg-Zn-Ca alloy wire by nanoparticles induced by extreme plastic deformation, Mater. Sci. Eng. 853 (2022) 143733.
[45] W. Ali, M. Echeverry-Rendón, G. Dominguez, K. van Gaalen, A. Kopp, C. González, J. Llorca, Bioabsorbable WE43 Mg alloy wires modified by continuous plasma electrolytic oxidation for implant applications. Part II: degradation and biological performance, Biomater. Adv. 147 (2023) 213325.
[46] Z. Cheng, S. Li, Y. Zhang, X. Wang, Q. Xie, K. Qian, Y. Shao, C. Chu, F. Xue, J. Bai, Research of a biodegradable Mg-5Zn wire for anastomosis staples, Mater. Lett. 352 (2023) 135173.
[47] Y. Zhang, J. Cao, M. Lu, Y. Shao, K. Jiang, X. Yang, X. Xiong, S. Wang, C. Chu, F. Xue, Y. Ye, J. Bai, A biodegradable magnesium surgical staple for colonic anastomosis: *in vitro* and *in vivo* evaluation, Bioact. Mater. 22 (2023) 225–238.
[48] S. Zhao, J.-M. Seitz, R. Eifler, H.J. Maier, R.J. Guillory, E.J. Earley, A. Drelich, J. Goldman, J.W. Drelich, Zn-Li alloy after extrusion and drawing: structural, mechanical characterization, and biodegradation in abdominal aorta of rat, Mater. Sci. Eng. C 76 (2017) 301–312.
[49] L. Wang, Y. He, H. Zhao, H. Xie, S. Li, Y. Ren, G. Qin, Effect of cumulative strain on the microstructural and mechanical properties of Zn-0.02 wt%Mg alloy wires during room-temperature drawing process, J. Alloys Compd. 740 (2018) 949–957.
[50] H. Guo, R.H. Cao, Y.F. Zheng, J. Bai, F. Xue, C.L. Chu, Diameter-dependent in vitro performance of biodegradable pure zinc wires for suture application, J. Mater. Sci. Technol. 35 (8) (2019) 1662–1670.
[51] J. Bai, Y. Xu, Q. Fan, R. Cao, X. Zhou, Z. Cheng, Q. Dong, F. Xue, Mechanical properties and degradation behaviors of Zn-xMg alloy fine wires for biomedical applications, Scanning 2021 (2021) 4831387.
[52] K. Chen, Y. Lu, H. Tang, Y. Gao, F. Zhao, X. Gu, Y. Fan, Effect of strain on degradation behaviors of WE43, Fe and Zn wires, Acta Biomater. 113 (2020) 627–645.
[53] M. Gao, D. Na, X. Ni, L. Song, I.P. Etim, K. Yang, L. Tan, Z. Ma, The mechanical property and corrosion resistance of Mg-Zn-Nd alloy fine wires *in vitro* and *in vivo*, Bioact. Mater. 6 (1) (2021) 55–63.
[54] M. Gao, K. Yang, L. Tan, Z. Ma, Improvement of mechanical property and corrosion resistance of Mg-Zn-Nd alloy by bi-direction drawing, J. Mater. Sci. Technol. 81 (2021) 88–96.
[55] M. Gao, I.P. Etim, K. Yang, L. Tan, Z. Ma, Enhancing mechanical property and corrosion resistance of Mg–Zn-Nd alloy wire by a combination of SPD techniques, extrusion and hot drawing, Mater. Sci. Eng. 829 (2022) 142058.
[56] M. Gao, K. Yang, L. Tan, Z. Ma, Role of bimodal-grained structure with random texture on mechanical and corrosion properties of a Mg-Zn-Nd alloy, J. Magnesium Alloys 10 (8) (2022) 2147–2157.
[57] W.-J. Lin, D.-Y. Zhang, G. Zhang, H.-T. Sun, H.-P. Qi, L.-P. Chen, Z.-Q. Liu, R.-L. Gao, W. Zheng, Design and characterization of a novel biocorrodible iron-based drug-eluting coronary scaffold, Mater. Des. 91 (2016) 72–79.
[58] M. Ghasri-Khouzani, J.R. McDermid, Effect of carbon content on the mechanical properties and microstructural evolution of Fe-22Mn-C steels, Mater. Sci. Eng. 621 (2015) 118–127.
[59] Y. Zhang, C. Roux, A. Rouchaud, A. Meddahi-Pellé, V. Gueguen, C. Mangeney, F. Sun, G. Pavon-Djavid, Y. Luo, Recent advances in Fe-based bioresorbable stents: materials design and biosafety, Bioact. Mater. 31 (2024) 333–354.
[60] H. Hermawan, H. Alamdari, D. Mantovani, D. Dubé, Iron-manganese: new class of metallic degradable biomaterials prepared by powder metallurgy, Powder Metall. 51 (1) (2008) 38–45.
[61] H. Hermawan, D. Dubé, D. Mantovani, Degradable metallic biomaterials: design and development of Fe-Mn alloys for stents, J. Biomed. Mater. Res. 93A (1) (2010) 1–11.
[62] S. Mandal, V. Kishore, M. Bose, S.K. Nandi, M. Roy, *In vitro* and *in vivo* degradability, biocompatibility and antimicrobial characteristics of Cu added iron-manganese alloy, J. Mater. Sci. Technol. 84 (2021) 159–172.
[63] Q. Wang, B. Zhang, Y. Ren, K. Yang, A self-healing stainless steel: role of nitrogen in eliminating detrimental effect of cold working on pitting corrosion resistance, Corrosion Sci. 145 (2018) 55–66.
[64] A.M. Quain, N.M. Khardori, Nutrition in wound care management: a comprehensive overview, Wounds 27 (12) (2015) 327–335.
[65] N. Yang, J. Venezuela, S. Almathami, M. Dargusch, Zinc-nutrient element based alloys for absorbable wound closure devices fabrication: current status, challenges, and future prospects, Biomaterials 280 (2022) 121301.
[66] E. Burlet, S.K. Jain, Manganese supplementation reduces high glucose-induced monocyte adhesion to endothelial cells and endothelial dysfunction in Zucker diabetic fatty rats, J. Biol. Chem. 288 (9) (2013) 6409–6416.
[67] H.M. Li, Z.B. Long, B. Han, Iron homeostasis and iron-related disorders, Chin. J. Hematol. 39 (9) (2018) 790–792.
[68] J. Zong, Q. He, Y. Liu, M. Qiu, J. Wu, B. Hu, Advances in the development of biodegradable coronary stents: a translational perspective, Mater. Today Bio. 16 (2022) 100368.
[69] D. Hernández-Escobar, S. Champagne, H. Yilmazer, B. Dikici, C.J. Boehlert, H. Hermawan, Current status and perspectives of zinc-based absorbable alloys for biomedical applications, Acta Biomater. 97 (2019) 1–22.
[70] L. Han, Z. Zhang, J. Dai, X. Li, J. Bai, Z. Huang, C. Guo, F. Xue, C. Chu, The influence of alternating cyclic dynamic loads with different low frequencies on the bio-corrosion behaviors of AZ31B magnesium alloy *in vitro*, Bioact. Mater. 7 (2022) 263–274.
[71] I. Kott, M. Lurie, The effects of electrosurgery and the surgical knife on the healing of intestinal anastomoses, Dis. Colon Rectum 16 (1) (1973) 33–38.
[72] C.A. Bundy, D.M. Jacobs, R.T. Zera, M.P. Bubrick, Comparison of bursting pressure of sutured, stapled and BAR anastomoses, Int. J. Colorectal Dis. 8 (1) (1993) 1–3.
[73] A. Oliveira, S. Faria, N. Gonçalves, A. Martins, P. Leão, Surgical approaches to colonic and rectal anastomosis: systematic review and meta-analysis, Int. J. Colorectal Dis. 38 (1) (2023) 52.